

Article

Terahertz Photoconductive Antenna Based on a Topological Insulator Nanofilm

Kirill A. Kuznetsov ¹, Daniil A. Safronenkov ¹, Petr I. Kuznetsov ² and Galiya Kh. Kitaeva ^{1,*}

¹ Faculty of Physics, Lomonosov Moscow State University, 119991 Moscow, Russia; kirill-spd@yandex.ru (K.A.K.); safronenkov.da14@physics.msu.ru (D.A.S.)

² Kotelnikov IRE RAS (Fryazino branch), 141190 Fryazino, Russia; pik218@fireras.su

* Correspondence: gkitaeva@physics.msu.ru

Abstract: In this study, the efficient generation of terahertz radiation by a dipole photoconductive antenna, based on a thin island film of a topological insulator, was experimentally demonstrated. The performance of the $\text{Bi}_{1.9}\text{Sb}_{0.1}\text{Te}_2\text{Se}$ antenna was shown to be no worse than those of a semiconductor photoconductive antenna, which is an order of magnitude thicker. The current–voltage characteristics were studied for the photo and dark currents in $\text{Bi}_{1.9}\text{Sb}_{0.1}\text{Te}_2\text{Se}$. The possible mechanisms for generating terahertz waves were analyzed by comparing the characteristics of terahertz radiation of an electrically biased and unbiased topological insulator.

Keywords: topological insulator; photoconductive antenna; terahertz waves



Citation: Kuznetsov, K.A.; Safronenkov, D.A.; Kuznetsov, P.I.; Kitaeva, G.K. Terahertz Photoconductive Antenna Based on a Topological Insulator Nanofilm. *Appl. Sci.* **2021**, *11*, 5580. <https://doi.org/10.3390/app11125580>

Academic Editor: Gennady M. Mikheev

Received: 14 May 2021
Accepted: 15 June 2021
Published: 16 June 2021

Publisher's Note: MDPI stays neutral with regard to jurisdictional claims in published maps and institutional affiliations.



Copyright: © 2021 by the authors. Licensee MDPI, Basel, Switzerland. This article is an open access article distributed under the terms and conditions of the Creative Commons Attribution (CC BY) license (<https://creativecommons.org/licenses/by/4.0/>).

1. Introduction

Currently, topological insulators (TIs) are considered to be promising new 2D materials for terahertz (THz) generators and detectors [1–3]. TIs are characterized by the presence of stable (topologically protected against backscattering), conducting surface states of an electronic gas. TIs can be used in the development of various interdisciplinary connections in many modern areas, including spintronics [4], laser physics [5], and quantum information [6].

Angle-resolved photoemission spectroscopy (ARPES) detects the presence of Dirac electrons with nondegenerate spins in many solids [7]. In addition to ARPES, there are other methods that are sensitive to edge electronic states. In [8], a new method was proposed for detecting the surface states of electrons based on the photo-electromagnetic effect (PEM), which is not sensitive to bulk conductivity. In [9], ultrafast manipulation of topologically enhanced surface transport was demonstrated using THz and mid-IR pulses in bismuth selenide. Correspondingly, the generation of THz radiation can also be sensitive to surface electron transfer. Hamh et al. demonstrated a circular anisotropy of the photon drag effect (PDE) in Bi_2Se_3 , which proves optical coupling with topological surface states [10].

In a number of previous studies, the generation of THz radiation under the action of pulsed optical pumping was investigated in bismuth chalcogenides of double [11,12] and quaternary [13] chemical compositions. A comprehensive review of the photovoltaic effects in Bi_2Te_3 and Sb_2Te_3 was given in [14]. A number of conclusions were drawn regarding the prevailing mechanisms of the generation of THz radiation, due to the excitation of photocurrents in the epitaxial films of topological insulators in the absence of any external electric bias field. In [15], it was shown that the contribution to the photocurrent from the PDE is an order of magnitude greater than the contribution from the diffusion current, and two times higher than the contribution from the drift current.

Topological insulators of quaternary compositions $\text{Bi}_{2-x}\text{Sb}_x\text{Te}_{3-y}\text{Se}_y$ are actively studied in connection with the possibility of smooth changes in their properties over a wide range. In [16], it was shown that there is a certain optimal curve (the “Ren’s curve”) in the composition–structure diagram $y(x)$, where the properties of electronic surface states are

most pronounced. This is associated with a significant suppression of the bulk contribution to the conductivity, as the actions of acceptors and donors cancel each other, which leads to the predominance of surface electron transport. $\text{Bi}_{2-x}\text{Sb}_x\text{Te}_{3-y}\text{Se}_y$ films with compositions located under the Ren's curve, as a rule, predominantly have p-type conductivity; while compositions located above this curve have conductivity of the n-type.

At present, research is continuing on the most efficient methods for generating and detecting terahertz radiation. Photoconductive semiconductor antennas are effective devices in the THz range for applications in spectroscopy, and various imaging and data transmission systems [17,18]. Due to the availability of components in the telecommunications industry, modern systems often use optical excitation at a wavelength of 1550 nm with femtosecond pulses of an erbium fiber laser [19,20]. Semiconductor structures, based on indium-gallium arsenide, were well studied as photoconductive materials for THz due to their suitable optical absorption wavelength of 1.5 μm . Recently, THz detectors fabricated from rhodium (Rh)-doped $\text{In}_{0.53}\text{Ga}_{0.47}\text{As}$ showed a record peak dynamic range of 105 dB and a bandwidth up to 6.5 THz [21]. A significant improvement in the characteristics of these devices was achieved with the help of such nanotechnological tools as plasmonic contact gratings, arrays of optical nanoantennas, optical nanocavities [22,23], and non-standard orientation of the substrates [24,25].

Another important area is the development and optimization of couplers at the output surfaces of photoconductive antennas. The performance of planar terahertz antennas can be improved by using hemispherical dielectric lenses. However, this increases the weight and volume of the antenna. Artificially created composite metamaterials have recently attracted considerable attention from both the scientific and engineering communities due to their unconventional properties [26–30].

It is also of interest to use various other photoconductive materials for their application in antennas pumped by telecom wavelength lasers. Singh et al. [31] presented a significantly ultra-broadband (extending up to 70 THz) THz emission from an Au-implanted Ge emitter that was compatible with mode-locked fiber lasers operating at wavelengths of 1.1 and 1.55 μm .

The development of new photoconductive nanomaterials for THz PCAs still remains a relevant and urgent task. In our previous work [32], we demonstrated amplification of the THz radiation power by applying a weak external electric field to a TI. In this work, we study the generation of a photoconductive antenna under the application of a strong bias external field.

2. Proposed System Design

A TI sample of $\text{Bi}_{1.9}\text{Sb}_{0.1}\text{Te}_2\text{Se}$ (BSTS) was prepared with a composition near the Ren's curve at the composition-structure diagram. It was grown by metalorganic vapor-phase epitaxy (MOVPE) on a (0001) sapphire substrate with a 10-nm zinc telluride (ZnTe) buffer layer of orientation (111) at the atmospheric pressure of hydrogen in a horizontal quartz reactor. The sources of organometallic compounds of bismuth, antimony, zinc, tellurium, selenium, trimethyl bismuth, trimethyl antimony, diethyl zinc, diethyl tellurium, and diethyl selenium were used. The ZnTe buffer layer was grown in one technological cycle with a BSTS film at a temperature of 463 $^{\circ}\text{C}$. To determine the elemental composition of the films, we used X-MaxN energy dispersive X-ray spectrometer with an electron microscope. A thin film of BSTS, 40 nm thick and of necessary composition, was selected for THz generation (Figure 1a).

A dipole antenna was fabricated by patterning Ti/Pd/Au metal electrodes (of corresponding thicknesses 50/120/200 nm) onto BSTS film. The gap between electrodes was 20 μm . Templates were preliminarily applied using the photolithography method. The fabricated TI-antenna had an impedance of 490 Ω . A hemispherical high-resistance silicon lens of 1 cm diameter was mounted on the surface of the Al_2O_3 substrate to collect the generated THz radiation (Figure 1c).

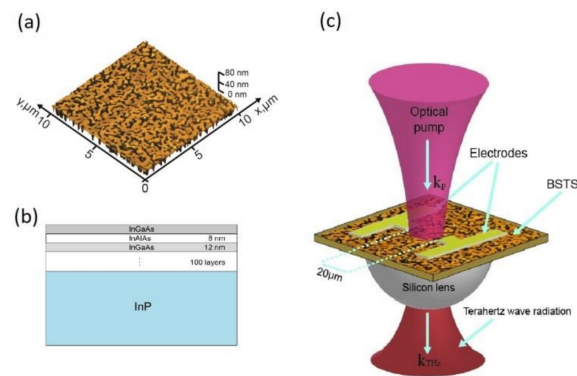


Figure 1. The (a) atomic force microscopy image of BSTS sample surface; (b) sketch of the InGaAs/InAlAs heterostructure; and (c) sketch of the antenna emitter.

To analyse the generation efficiency, we compared the generated THz pulses from two photoconductive antennas with the same dipole structure, one fabricated on the BSTS film (TI PCA) and the other on a semiconductor multilayer heterostructure (semiconductor PCA). Another dipole photoconductive antenna, fabricated on a low-temperature grown $\text{In}_{0.5}\text{Ga}_{0.5}\text{As}/\text{In}_{0.5}\text{Al}_{0.5}\text{As}$ superlattice, was used as a second antenna for reference. The parameters of similar spiral antenna were previously studied and reported in [33]. The multilayer heterostructure InGaAs/InAlAs for semiconductor PCA was grown on an InP (111) substrate (Figure 1b). Such structures are usually prepared by molecular beam epitaxy and exhibit a high conversion efficiency of optical radiation into the broadband THz radiation. The overall thickness of the InGaAs/InAlAs heterostructure was 2000 nm, and the total thickness of all InGaAs layers was 1200 nm. An impedance semiconductor PCA was 12.8 k Ω .

We measured the room temperature absorption coefficient at the pump wavelength. It was 4300 cm^{-1} for our InGaAs layer lattice and 120,000 cm^{-1} for the BSTS sample. In both cases, the thickness of the antenna material was less than the pump field penetration depth. Thus, the selected film thicknesses, 40 nm in the case of BSTS and 1200 nm of the total thickness of the InGaAs layers, provided almost uniform pumping illumination throughout the depth of the samples.

Figure 2a shows a photograph of the board. The electrodes were deposited on the samples of photoconductive films with five dipole gaps (Figure 2b). One of the five inter-electrode gaps, located above the most homogeneous region in the case of the topological insulator nanofilm, was chosen. Then, by heating with hot air from a soldering station, the electrodes were soldered to the board. A photograph of electrodes under a microscope is shown in Figure 2c. A hemispherical high-resistivity silicon lens 1 cm in diameter was pressed onto the substrate from above.

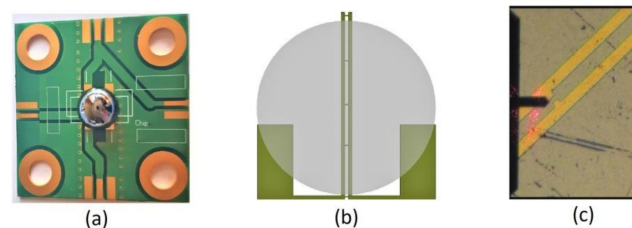


Figure 2. A (a) photo of the circuit board assembly; (b) sketch of the electrodes, with the gray circle representing the projection of the silicon lens onto the plane of the electrodes; and (c) image of the inter-electrode gap under a microscope. The gap width is 20 μm .

The measurements of THz generation characteristics were conducted on an experimental setup schematically presented in Figure 3. An Er^{3+} fiber laser was used as a source for optical pulsed pumping at a wavelength of 1560 nm, pulse repetition rate of 70 MHz,

and pulse duration of 100 fs. Eighty percent of the radiation power (approximately 100 mW in the average intensity) was directed onto the antenna under study, and the last 20% of the radiation was used to run a commercial (Menlo Systems) semiconductor heterostructure photoconductive antenna. The latter was used for the detection of the waveforms of emitted THz fields. The pump beam was focused on the TI PCA1 with a short-focus (5 mm) lens. The parabolic mirrors collected the THz radiation and focused it on the input silicon lens of the antenna-detector PCA2.

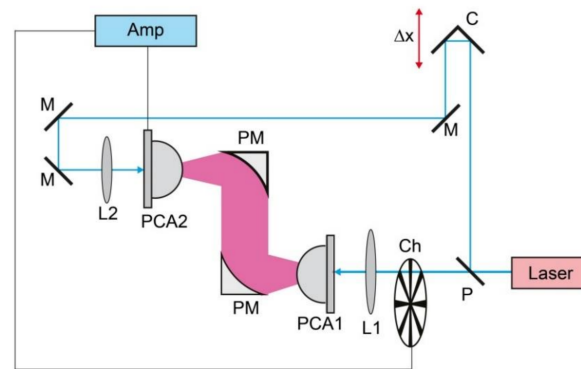


Figure 3. Schematics of the terahertz time-domain spectroscopy setup.

The photocurrents from the PCAs' were measured by a micro-ammeter and by a lock-in-amplifier at different bias voltages and laser pump powers. Sufficiently high photocurrents were measured simultaneously by using a current-sensitive input of the lock-in-amplifier. After the calibration of the lock-in-amplifier output data in microamperes, this sensitive device was used for measuring the lower photocurrents against a background of significant dark currents.

3. Results

A waveform of THz radiation, recorded from TI PCA at a bias voltage of 20 V, and its spectrum, obtained using fast Fourier transform, are shown by red curves in Figure 4a,b, respectively. The spectra in Figure 4b are "bumpy" due to re-reflection in the substrates and absorption by the water vapor. They extend up to 2 THz, which corresponds to the spectral range of the antenna-detector. The dynamic range of the obtained TI PCA radiation was approximately 60 dB.

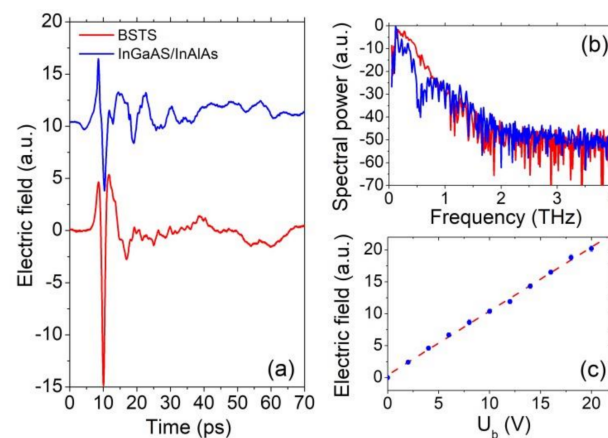


Figure 4. The (a) time-domain waveforms of dipole antennas based on BSTS (red) and InGaAs/InAlAs (blue); (b) fast Fourier transform spectra of BSTS (red) and InGaAs/InAlAs (blue) antennas; and (c) THz electric field amplitude versus bias voltage for BSTS antenna.

The blue curve in Figure 4a shows a waveform of THz radiation from a similar dipole semiconductor PCA biased at the same voltage $U = 20$ V (the curves were vertically shifted artificially). Though the thicknesses of active media differed by almost an order of magnitude (40 nm and 2000 nm), the amplitudes of the generated THz fields were comparable to each other. Even the peak-to-peak amplitude was 1.5 times more in case of thin TI PCA. Hence, we can conclude that, with the unit thickness of the medium, generation using BSTS is much more efficient than that using InGaAs/InAlAs. Figure 4c shows the dependence of the electric field amplitude on the bias voltage for TI PCA. The linear character of this dependence is clearly seen in the wide voltage range. At higher voltages, the THz signal was not recorded to avoid possible damage to the sample due to electrical breakdown.

As the generated photocurrents are responsible for the generation of THz radiation, it was interesting to measure them in the range of acting bias voltages of 0–20 V. First, the steady current-voltage characteristic was recorded, i.e., the dependence of the dark current on the voltage in the absence of incident optical pumping (Figure 5a). This characteristic was well approximated up to 13 V by a linear curve. However, at higher voltages some deviation from the linear fit was observed, which can be explained by a decrease in the resistance of the sample due to heating. We recorded the heating of the BSTS from room temperature to 50 °C by a thermocouple at a maximal bias voltage, $U_b = 20$ V. Figure 5b demonstrates the dependence of the average photocurrent on the bias voltage. It was also well described by a linear law over the entire range of U_b . For comparison, a similar dependence was shown for the semiconductor antenna, which lies well below the curve for the TI PCA. Figure 5c shows the obtained dependence of the TI PCA photocurrent on the pump power. It is linear; this is a typical situation for photoconductive antennas operating far from breakdown voltages and carrier screening effects.

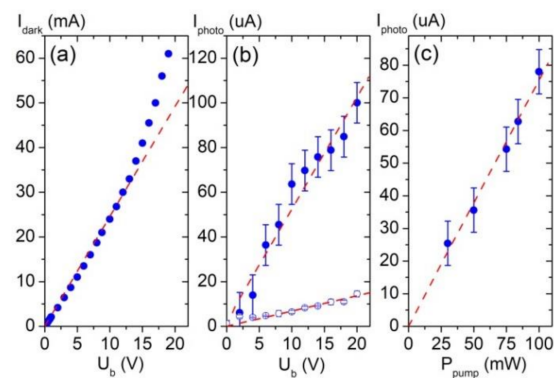


Figure 5. The (a) I-V characteristic of TI PCA measured without pump radiation; (b) filled circles: voltage dependence of the time-averaged photo-excited current of TI PCA; open circles: the same dependence for InGaAs/InAlAs PCA; and (c) dependence of the time-averaged photo-excited current on the pump power for TI PCA.

Figure 6a demonstrates the phase change of the generated THz radiation by 180° when the polarity of the bias voltage $U_b = 15$ V was reversed. If we summarize the two signals obtained at inverse voltages, we realise practically the same waveform as in the absence of an external voltage (Figure 6b). Similar results were observed at a higher voltage of 20 V.

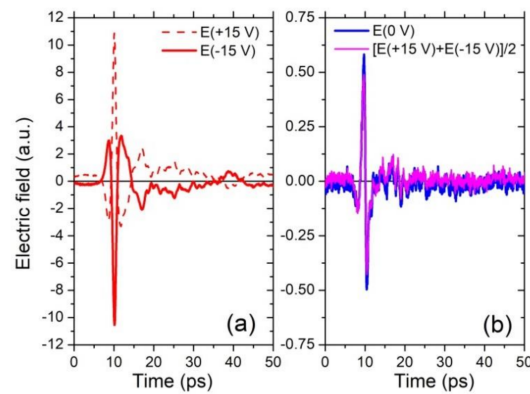


Figure 6. The (a) THz pulses at opposite bias voltages; and (b) comparison of the unbiased THz pulse (blue) with the result of averaging of two waveforms from oppositely biased antennas (magenta).

4. Discussion

In general, a fairly large set of different mechanisms can be used to explain THz generation in TIs of double and quaternary compositions. The most instantaneous one is direct optical rectification of the laser pump field [11] due to nonlinear polarization.

$$\mathbf{P}(t) \sim \int_{-\infty}^t \hat{\chi}^{(2)}(t-t', t-t'') : \mathbf{E}(t') \mathbf{E}^*(t'') dt' dt'' + c.c. \quad (1)$$

Here, $\mathbf{E}(t)$ stands for the laser pump field and $\hat{\chi}^{(2)}$ describes the second-order nonlinear-optical susceptibility. Due to the centrosymmetric structure of TI volume, the components of $\hat{\chi}^{(2)}$ tensor are non-zero only at its surface and, thus, this effect is related specifically to surface excitations. However, its contribution was much smaller [34] than the THz field generated by transient currents of photo-induced charge carriers. The current-induced THz field depends on time derivatives of the two types of photocurrents, usually referred as linear (\mathbf{j}_L) and nonlinear (\mathbf{j}_{NL}) ones [15]:

$$\mathbf{E}_{THz}(t) \sim \frac{\partial \mathbf{j}_L(t)}{\partial t} + \frac{\partial \mathbf{j}_{NL}(t)}{\partial t}. \quad (2)$$

In the frame of the simplest classical description, both types of currents should depend on temporal behaviour of the carrier's concentration $N(t)$, mobility μ , and some specific field $\tilde{\mathbf{E}}$ as:

$$\mathbf{j}_{L,NL}(t) = e\mu N(t) \tilde{\mathbf{E}}. \quad (3)$$

In our case of above-bandgap photo-excitation, the amplitude of the $N(t)$ pulse scaled up with the pump pulse energy. As was reasonably argued in [35], the contribution from photo-induced electrons to both types of currents in BSTS was considerably more than the contribution from holes. A presence of non-zero dc field is necessary for directional motion of charge carriers in this description, regardless of whether it is applied externally or originates due to specific internal processes. The origin of, and the character of its possible temporal variation, are different for different THz generation mechanisms.

In case of linear currents \mathbf{j}_L , the temporal variation of $\tilde{\mathbf{E}}$ was negligible. In a photoconductive antenna, $\tilde{\mathbf{E}} = \mathbf{E}_{dc}$ is created by an external bias voltage source. With significantly smaller magnitudes, $\tilde{\mathbf{E}}$ also exists as a surface depletion field or due to the photo-Dember effect [15], regardless of whether an additional lateral external field is applied. The surface depletion and photo-Dember fields are directed along the normal to the TI surface and determine the motion of volume carriers even in case of zero applied voltage. In addition, some surface built-in field can exist in the lateral direction and be responsible for the specific contribution of surface carriers to THz generation. For all generation effects caused by different-type linear currents, the THz waveforms should have almost the same shape,

repeating the shape of $\partial N(t)/\partial t$. This shape is clearly presented in waveforms like those in Figure 6a. The waveforms were obtained in the case where the high external bias field made \mathbf{j}_L more than other nonlinear contributions to the net photo-induced current. It was seen that changing the bias voltage sign did not cause any observable changes in the THz field magnitude, apart from reversing its sign. Moreover, both curves in Figure 6b demonstrate the zero residual THz field at delay times, when contribution of linear currents should be maximal. Thus, we concluded that the effects of lateral and longitudinal built-in fields were negligible at zero voltage, and were not linearly enhanced when the bias voltage was applied to the TI antenna.

By comparing the mean photocurrents detected in the TI antenna and the semiconductor PCA at the same bias voltage (Figure 5b), we obtained a ratio between the photocurrents ($\sim 1:7$), which roughly corresponded to the ratio between the mobilities of bulk photoelectrons in both materials, $\mu_{semi} = 30 \text{ cm}^2/(\text{V} \cdot \text{s})$ in our semiconductor InGaAs/InAlAs superlattice [33], and $\mu_{TI} = 166 \text{ cm}^2/(\text{V} \cdot \text{s})$ in BSTS [36]. According to (3) this meant that the mean concentrations of photo-induced bulk electrons were the same in both materials. However, the peak-to-peak THz field amplitudes detected in TI and semiconductor PCAs (Figure 4a) referred to each other as 1.6:1. This indicates that the photocurrent change rate in BSTS was smaller than in the InGaAs/InAlAs superlattice. Thus, we estimated the ratio between the electron relaxation times in the both materials as $\tau_{TI}/\tau_{semi} \sim (E_{THz,semi}/E_{THz,TI})(\mu_{TI}/\mu_{semi}) \sim 3.5$. Taking the previously measured value of the characteristic relaxation time for the InGaAs/InAlAs superlattice $\tau_{semi} = 1.7 \text{ ps}$, we obtained the relaxation time for the bulk photo-induced electrons in BSTS as approximately $\tau_{TI} \approx 6 \text{ ps}$.

Let us consider which relaxation process this time describes. In the case of BSTS, with extremely low initial concentration of free bulk carriers, the THz generation process began with the absorption of pump photons and the formation of electrons in the conduction band (Figure 7). The characteristic time of this process was of the order of the pump duration t_0 . Time t_1 was of the order of a few picoseconds and, within this interval, a relaxation of bulk electrons took place due to the phonon emission [37]. The second type of relaxation process was an interband transition from the bulk conduction band to the surface states at the Dirac cone. As the Fermi level E_f lies in the band of surface states (SSs) in a BSTS with a composition near the Ren's curve, SSs above E_f were primarily unoccupied. The characteristic time t_2 of this process is rather long, approximately 5–10 ps [37,38]. Finally, the relaxation of SSs was the third relaxation mechanism, with time t_3 as hundreds of femtoseconds or several picoseconds [9,39]. The direct interband transitions from the conduction band to the valence band are rather long and usually last from hundreds to thousands of picoseconds. These slow processes do not significantly contribute to generation at THz frequencies. Our estimate of the relaxation time corresponds to t_2 . Thus, we concluded that the process of population of the edge states by photo-induced bulk electrons made up the main contribution to the formation of the THz generation spectrum of the BSTS TI PCA.

The nonlinear \mathbf{j}_{NL} currents are known to appear in unbiased TIs due to photo-galvanic (PG) and photon-drag (PD) effects [10–15,40,41]. Currents induced in these processes should quadratically depend on the laser pump field, both under sub-bandgap excitation [40] and under above-bandgap [10,13] laser excitation. Phenomenologically, dependences of these currents on the laser electric field for the non-stationary case [42] are described as:

$$\mathbf{j}_{NL}^{PG}(t) = \int_{-\infty}^t \widehat{\beta}(t-t', t-t'') : \mathbf{E}(t') \mathbf{E}^*(t'') dt' dt'' + c.c., \quad (4)$$

$$\mathbf{j}_{NL}^{PD}(t) = \int_{-\infty}^t \widehat{\gamma}(t-t', t-t'') : \mathbf{E}(t') \frac{\partial \mathbf{E}^*(t'')}{\partial \mathbf{r}} dt' dt'' + c.c. \quad (5)$$

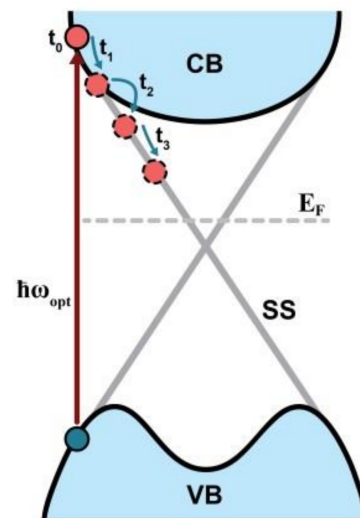


Figure 7. Relaxation of carriers in BSTS film.

The PG effect takes place due to third-order tensor $\widehat{\beta}(t-t', t-t'')$, which is non-zero only at the surface of TI. It is tied directly to the specific surface carriers, while both the bulk and surface electrons take part in PD effect via the fourth-order tensor $\widehat{\gamma}(t-t', t-t'')$. As it was shown in previous experimental works [40,41], in case of the normal incidence of the pump beam on BSTS, PD effect is negligible in comparison with PG generation. In our case, at zero bias voltage we detected the same bipolar shapes of the temporal waveforms (Figure 6b) as in [15]. Thus, we can relate the THz fields observed in the unbiased TI to the PG effect.

By comparing expression (4) for PG current with the general presentation of the induced currents in form (3), one can see that (4) seemingly depicts an effect of resonant nonlinear generation of an effective field $\widetilde{\mathbf{E}}$, which is responsible for the directional motion of free carriers. More accurate calculations, performed by considering the kinetic Boltzmann distribution equation for the electron distribution function within the semi-classical approach [40], can be treated so that an effective field $\widetilde{\mathbf{E}}$ appears here as a result of two processes: an alignment of carrier moments along the pump electric field, and an asymmetric scattering of carriers at the surface of TI [41]. However, this theory describes quadratic dependence on the pump field for THz field generated under below-bandgap excitation, but needs further assumptions to explain generation under above-bandgap pumping.

Indeed, the below-bandgap excitation did not change the carrier's concentration, $N(t)$ was almost constant in (3), and only the temporal change of effective $\widetilde{\mathbf{E}}$ determined a short PG current pulse, which scaled up quadratically with the pump electric field. At the same time, when the pump photon energy exceeded the bandgap, the concentration of charge carriers also grew quadratically with the pump field. This was the case for bulk electrons, while a saturation of the concentration of the surface electrons may occur. However, no fourth-order dependence on the pump field was observed under above-bandgap excitation.

So, taking all the above considerations into account, we can conclude that: (1) the impact of the PG effect, and accompanying effective PG field $\widetilde{\mathbf{E}}$, into THz generation in the biased THz antenna was negligible. Generation occurred due to photo-excited *bulk* carriers and its relaxation through the surface states in the presence of the constant field \mathbf{E}_{dc} . The temporal shape of $N(t)$ determined THz generation waveform and the width of the antenna spectral response; and (2) in the absence of an external biased field, THz generation took place due to the PG effect by *surface* electrons, which had almost the same concentration during the whole generation pulse. The temporal shape of effective $\widetilde{\mathbf{E}}(t)$ determined the THz generation specific waveform and the width of the BSTS spectral response.

5. Conclusions

In conclusion, we demonstrated a working photoconductive antenna with a dynamic range of order of 60 dB based on the nanofilm of the TI $\text{Bi}_{2-x}\text{Sb}_x\text{Te}_{3-y}\text{Se}_y$. In addition to the known nonlinear effects, the photoconductive mechanism of THz generation was realized in TIs because of the relaxation of bulk electrons through the surface states. A comparison of photoconductive antennas based on TI and semiconductor heterostructure showed that, despite the great difference in the thicknesses by more than one order, the THz fields of both PCAs were comparable in amplitude. The time-averaged photocurrent and dark currents arising in the TI PCA were measured and their linear dependences on the bias voltage were demonstrated.

TI antennas represent promising tools for generating THz radiation. Due to being extremely thin, they can be easily integrated into nanophotonic devices. They are inexpensive to manufacture, as the growing of a TI film takes several minutes without the need for difficult growth conditions, such as those required for MBE-technology. Their conversion efficiency can be further increased by applying plasmon gratings. Lastly, TI antennas are able to withstand large dark currents without being destroyed.

Author Contributions: Conceptualization, K.A.K., and P.I.K.; methodology, G.K.K.; software, D.A.S.; validation, K.A.K., and D.A.S.; formal analysis, G.K.K.; investigation, K.A.K., D.A.S., and G.K.K.; sample growth and characterization, P.I.K.; writing—original draft preparation, K.A.K., and G.K.K.; writing—review and editing, K.A.K., G.K.K., and D.A.S.; visualization, D.A.S.; funding acquisition, K.A.K. All authors have read and agreed to the published version of the manuscript.

Funding: This research was funded by the Russian Foundation of Basic Research, grant numbers 18-29-20101 and 19-02-00598.

Institutional Review Board Statement: Not applicable.

Informed Consent Statement: Not applicable.

Acknowledgments: The authors are grateful to D.S. Ponomarev, A.N. Klochkov, D.V. Lavrukhin, V.B. Novikov, and S.N. Molotkov for helpful discussions.

Conflicts of Interest: The authors declare no conflict of interest.

References

1. Zhang, X.; Wang, J.; Zhang, S.-C. Topological insulators for high-performance terahertz to infrared applications. *Phys. Rev. B* **2010**, *82*, 245107. [[CrossRef](#)]
2. Viti, L.; Coquillat, D.; Politano, A.; Kokh, K.A.; Aliev, Z.S.; Babanly, M.B.; Tereshchenko, O.E.; Knap, W.; Chulkov, E.V.; Vitiello, M.S. Plasma-Wave Terahertz Detection Mediated by Topological Insulators Surface States. *Nano Lett.* **2016**, *16*, 80–87. [[CrossRef](#)]
3. West, D.; Zhang, S.B. Thin-film topological insulators for continuously tunable terahertz absorption. *Appl. Phys. Lett.* **2018**, *112*, 091601. [[CrossRef](#)]
4. Li, C.H.; van 't Erve, O.M.J.; Yan, C.; Li, L.; Jonker, B.T. Electrical detection of current generated spin in topological insulator surface states: Role of interface resistance. *Sci. Rep.* **2019**, *9*, 6906. [[CrossRef](#)] [[PubMed](#)]
5. Yan, P.; Lin, R.; Ruan, S.; Liu, A.; Chen, H.; Zheng, Y.; Chen, S.; Guo, C.; Hu, J. A practical topological insulator saturable absorber for mode-locked fiber laser. *Sci. Rep.* **2015**, *5*, 1–5. [[CrossRef](#)] [[PubMed](#)]
6. He, M.; Sun, H.; He, Q.L. Topological insulator: Spintronics and quantum computations. *Front. Phys.* **2019**, *14*, 43401. [[CrossRef](#)]
7. Ando, Y. Topological Insulator Materials. *J. Phys. Soc. Jpn.* **2013**, *82*, 102001. [[CrossRef](#)]
8. Egorova, S.G.; Chernichkin, V.I.; Ryabova, L.I.; Skipetrov, E.P.; Yashina, L.; Danilov, S.N.; Ganichev, S.D.; Khokhlov, D.R. Detection of highly conductive surface electron states in topological crystalline insulators $\text{Pb}_{1-x}\text{Sn}_x\text{Se}$ using laser terahertz radiation. *Sci. Rep.* **2015**, *5*, 11540. [[CrossRef](#)] [[PubMed](#)]
9. Luo, L.; Yang, X.; Liu, X.; Liu, Z.; Vaswani, C.; Cheng, D.; Mootz, M.; Zhao, X.; Yao, Y.; Wang, C.-Z.; et al. Ultrafast manipulation of topologically enhanced surface transport driven by mid-infrared and terahertz pulses in Bi_2Se_3 . *Nat. Commun.* **2019**, *10*, 1–9. [[CrossRef](#)]
10. Hamh, S.Y.; Park, S.-H.; Jerng, S.-K.; Jeon, J.H.; Chun, S.-H.; Lee, J.S. Helicity-dependent photocurrent in a Bi_2Se_3 thin film probed by terahertz emission spectroscopy. *Phys. Rev. B* **2016**, *94*, 161405. [[CrossRef](#)]
11. Zhu, L.-G.; Kubera, B.; Mak, K.F.; Shan, J. Effect of Surface States on Terahertz Emission from the Bi_2Se_3 Surface. *Sci. Rep.* **2015**, *5*, 1–8. [[CrossRef](#)] [[PubMed](#)]

12. Tu, C.-M.; Chen, Y.-C.; Huang, P.; Chuang, P.-Y.; Lin, M.-Y.; Cheng, C.-M.; Lin, J.-Y.; Juang, J.-Y.; Wu, K.-H.; Huang, J.-C.A.; et al. Helicity-dependent terahertz emission spectroscopy of topological insulator Sb_2Te_3 thin films. *Phys. Rev. B* **2017**, *96*, 195407. [[CrossRef](#)]
13. Onishi, Y.; Ren, Z.; Novak, M.; Segawa, K.; Ando, Y.; Tanaka, K. Instantaneous Photon Drag Currents in Topological Insulators. *arXiv* **2014**, arXiv:1403.2492.
14. Plank, H.; Pernul, J.; Gebert, S.; Danilov, S.N.; König-Otto, J.; Winnerl, S.; Lanius, M.; Kampmeier, J.; Mussler, G.; Aguilera, I.; et al. Infrared/terahertz spectra of the photogalvanic effect in (Bi,Sb)Te based three-dimensional topological insulators. *Phys. Rev. Mater.* **2018**, *2*, 024202. [[CrossRef](#)]
15. Fang, Z.; Wang, H.; Wu, X.; Shan, S.; Wang, C.; Zhao, H.; Xia, C.; Nie, T.; Miao, J.; Zhang, C.; et al. Non-linear terahertz emission in the three-dimensional topological insulator Bi_2Te_3 by terahertz emission spectroscopy. *Appl. Phys. Lett.* **2019**, *115*, 191102. [[CrossRef](#)]
16. Ren, Z.; Taskin, A.A.; Sasaki, S.; Segawa, K.; Ando, Y. Optimizing $\text{Bi}_{2-x}\text{Sb}_x\text{Te}_{3-y}\text{Se}_y$ solid solutions to approach the intrinsic topological insulator regime. *Phys. Rev. B* **2011**, *84*, 165311. [[CrossRef](#)]
17. Castro-Camus, E.; Alfaro, M. Photoconductive devices for terahertz pulsed spectroscopy: A review. *Photon. Res.* **2016**, *4*, A36. [[CrossRef](#)]
18. Burford, N.M.; El-Shenawee, M.O. Review of terahertz photoconductive antenna technology. *Opt. Eng.* **2017**, *56*, 010901. [[CrossRef](#)]
19. Vieweg, N.; Rettich, F.; Deninger, A.; Roehle, H.; Dietz, R.; Göbel, T.; Schell, M. Terahertz-time domain spectrometer with 90 dB peak dynamic range. *J. Infrared Millim. Terahertz Waves* **2014**, *35*, 823–832. [[CrossRef](#)]
20. Globisch, B.; Dietz, R.J.B.; Kohlhaas, R.B.; Göbel, T.; Schell, M.; Alcer, D.; Semtsiv, M.; Masselink, W.T. Iron doped InGaAs: Competitive THz emitters and detectors fabricated from the same photoconductor. *J. Appl. Phys.* **2017**, *121*, 053102. [[CrossRef](#)]
21. Kohlhaas, R.B.; Breuer, S.; Nellen, S.; Liebermeister, L.; Schell, M.; Semtsiv, M.P.; Masselink, W.T.; Globisch, B. Photo-conductive terahertz detectors with 105 dB peak dynamic range made of rhodium doped InGaAs featured. *Appl. Phys. Lett.* **2019**, *114*, 221103. [[CrossRef](#)]
22. Lepeshov, S.; Gorodetsky, A.; Krasnok, A.; Rafailov, E.; Belov, P. Enhancement of terahertz photoconductive antenna operation by optical nanoantennas. *Laser Photonics Rev.* **2017**, *11*, 1600199. [[CrossRef](#)]
23. Yachmenev, A.E.; Lavrukhin, D.V.; Glinskiy, I.A.; Zenchenko, N.V.; Goncharov, Y.G.; Spektor, I.E.; Khabibullin, R.A.; Otsuji, T.; Ponomarev, D.S. Metallic and dielectric metasurfaces in photoconductive terahertz devices: A review. *Opt. Eng.* **2019**, *59*, 061608. [[CrossRef](#)]
24. Kuznetsov, K.A.; Galiev, G.B.; Kitaeva, G.K.; Kornienko, V.V.; Klimov, E.A.; Klochkov, A.N.; Leontyev, A.A.; Pushkarev, S.S.; Malrsev, P.P. Photoconductive antennas based on epitaxial films $\text{In}_{0.5}\text{Ga}_{0.5}\text{As}$ on GaAs (111)A and (100)A substrates with a metamorphic buffer. *Laser Phys. Lett.* **2018**, *15*, 076201. [[CrossRef](#)]
25. Galiev, G.B.; Grekhov, M.M.; Kitaeva, G.K.; Klimov, E.A.; Klochkov, A.; Kolentsova, O.S.; Kornienko, V.; Kuznetsov, K.A.; Maltsev, P.; Pushkarev, S. Terahertz-radiation generation in low-temperature InGaAs epitaxial films on (100) and (411) InP substrates. *Semiconductors* **2017**, *51*, 310–317. [[CrossRef](#)]
26. Zhang, Q.-L.; Si, L.-M.; Huang, Y.; Lv, X.; Zhu, W. Low-index-metamaterial for gain enhancement of planar terahertz antenna. *AIP Adv.* **2014**, *4*, 037103. [[CrossRef](#)]
27. Hussain, N.; Nguyen, T.K.; Han, H.; Park, I. Minimum Lens Size Supporting the Leaky-Wave Nature of Slit Dipole Antenna at Terahertz Frequency. *Int. J. Antennas Propag.* **2016**, *2016*, 1–8. [[CrossRef](#)]
28. Hussain, N.; Park, I. Design of a wide-gain-bandwidth metasurface antenna at terahertz frequency. *AIP Adv.* **2017**, *7*, 055313. [[CrossRef](#)]
29. Llombart, N.; Chattopadhyay, G.; Skalare, A.; Mehdi, I. Novel Terahertz Antenna Based on a Silicon Lens Fed by a Leaky Wave Enhanced Waveguide. *IEEE Trans. Antennas Propag.* **2011**, *59*, 2160–2168. [[CrossRef](#)]
30. Li, X.; Yin, W.; Khamas, S. An Efficient Photomixer Based Slot Fed Terahertz Dielectric Resonator Antenna. *Sensors* **2021**, *21*, 876. [[CrossRef](#)]
31. Singh, A.; Pashkin, A.; Winnerl, S.; Welsch, M.; Beckh, C.; Sulzer, P.; Leitenstorfer, A.; Helm, M.; Schneider, H. Up to 70 THz bandwidth from an implanted Ge photoconductive antenna excited by a femtosecond Er:fibre laser. *Light. Sci. Appl.* **2020**, *9*, 1–7. [[CrossRef](#)]
32. Kuznetsov, K.A.; Kitaeva, G.K.; Kuznetsov, P.I.; Yakushcheva, G.G. Generation of terahertz radiation from the island films of topological insulator $\text{Bi}_{2-x}\text{Sb}_x\text{Te}_{3-y}\text{Se}_y$. *AIP Adv.* **2019**, *9*, 015310. [[CrossRef](#)]
33. Kuznetsov, K.; Klochkov, A.; Leontyev, A.; Klimov, E.; Pushkarev, S.; Galiev, G.; Kitaeva, G. Improved InGaAs and InGaAs/InAlAs Photoconductive Antennas Based on (111)-Oriented Substrates. *Electronics* **2020**, *9*, 495. [[CrossRef](#)]
34. Braun, L.; Mussler, G.; Hruban, A.; Konczykowski, M.; Schumann, T.; Wolf, M.; Münzenberg, M.; Perfetti, L.; Kampfrath, T. Ultrafast photocurrents at the surface of the three-dimensional topological insulator Bi_2Se_3 . *Nat. Commun.* **2016**, *7*, 13259. [[CrossRef](#)]
35. Park, S.H.; Hamh, S.Y.; Park, J.; Kim, J.S.; Lee, J.S. Possible flat band bending of the $\text{Bi}_{1.5}\text{Sb}_{0.5}\text{Te}_{1.7}\text{Se}_{1.3}$ crystal cleaved in an ambient air probed by terahertz emission spectroscopy. *Sci. Rep.* **2016**, *6*, 36343. [[CrossRef](#)]
36. Kuznetsov, K.A.; Kuznetsov, P.I.; Frolov, A.D.; Kovalev, S.P.; Ilyakov, I.E.; Ezhov, A.A.; Kitaeva, G.K. Bulk and surface terahertz conductivity of $\text{Bi}_{2-x}\text{Sb}_x\text{Te}_{3-y}\text{Se}_y$ topological insulators. *Opt. Eng.* **2021**, *60*, 082012. [[CrossRef](#)]

37. Lorenc, M.; Onishi, Y.; Ren, Z.; Segawa, W.; Kaszub, W.; Ando, Y.; Tanaka, K. Ultrafast carrier relaxation through Auger recombination in the topological insulator $\text{Bi}_{1.5}\text{Sb}_{0.5}\text{Te}_{1.7}\text{Se}_{1.3}$. *Phys. Rev. B* **2015**, *91*, 085306. [[CrossRef](#)]
38. Sobota, J.A.; Yang, S.; Analytis, J.G.; Chen, Y.L.; Fisher, I.R.; Kirchmann, P.S.; Shen, Z.-X. Ultrafast Optical Excitation of a Persistent Surface-State Population in the Topological Insulator Bi_2Se_3 . *Phys. Rev. Lett.* **2012**, *108*, 117403. [[CrossRef](#)]
39. Kovalev, S.; Tielrooij, K.-J.; Deinert, J.-C.; Ilyakov, I.; Awari, N.; Chen, M.; Ponomaryov, A.; Bawatna, M.; de Oliveira, T.V.A.G.; Eng, L.M.; et al. Terahertz signatures of ultrafast Dirac fermion relaxation at the surface of topological insulators at room temperature. *arXiv* **2006**, arXiv:2006.03948.
40. Plank, H.; Ganichev, S.D. A review on terahertz photogalvanic spectroscopy of Bi_2Te_3 - and Sb_2Te_3 -based three dimensional topological insulators. *Solid State Electron.* **2018**, *147*, 44–50. [[CrossRef](#)]
41. Plank, H.; Golub, L.E.; Bauer, S.; Bel'kov, V.V.; Herrmann, T.; Olbrich, P.; Eschbach, M.; Plucinski, L.; Schneider, C.M.; Kampmeier, J.; et al. Photon drag effect in $(\text{Bi}_{1-x}\text{Sb}_x)_2\text{Te}_3$ three-dimensional topological insulators. *Phys. Rev. B* **2016**, *93*, 125434. [[CrossRef](#)]
42. Il'inskii, Y.A.; Keldysh, L.V. General Theory of Interaction of Electromagnetic Fields with Matter. In *Electromagnetic Response of Material Media*; Springer: Boston, MA, USA, 1994.